A wavelet based numerical simulation of Navier-Stokes equations under uncertainty

Souleymane Kadri Harouna, Etienne Mémin

A wavelet based numerical simulation of Navier-Stokes equations under uncertainty

Souleymane Kadri Harouna* and Étienne Mémin†

In this work we explore the numerical simulation of Navier-Stokes equations representation incorporating an uncertainty component on the fluid flow velocity. The uncertainty considered is formalized through a random field uncorrelated in time but correlated in space. This model enables the constitution of large scale dynamical models of the flows in which emerges an anisotropic subgrid tensor reminiscent to the Reynolds stress tensor. This subgrid model is directly related to the uncertainty variance tensor. This property allows us to propose simple models of this stress tensor that are computed directly on the resolved component. These models are here assessed on a standard Green-Taylor vortex at Reynolds 1600 and on a Crow instability at Reynolds 3200. We also describe in this paper an efficient divergence free wavelet scheme for the numerical simulation of this model. The stability condition of the divergence-free wavelet based numerical scheme we used in this study is also discussed.

1. Introduction

The large scale analysis of complex fluid flows in domains ranging from climate sciences to engineering sciences requires to constitute dynamics models incorporating properly contributions that are difficult to specify precisely at the envisaged resolution scale. This includes for instance physical phenomena generating a forcing at small scale or the action of boundary layers, but also partially known inlet or boundary conditions, and eventually numerical errors arising from truncation policy and scale coarsening procedures. An accurate deterministic modeling of the effects of these processes is obviously hardly achievable in complex situations and we advocate instead the use of a stochastic modeling. Within this prospect, we aim at describing these missing contributions as random variables that will be referred to as flow uncertainties in the following. The modeling of such uncertainties but also of their evolution along time is of the utmost importance in ensemble methods used in geophysics, either for data assimilation or forecasting issues. In both cases, a modeling of the flow dynamics errors enables to rank the quality of some flow configurations. This authorizes ideally to set up efficient filtering strategies in which high errors are corrected by more meaningful data.

These errors or uncertainties are meant to represent principally small-scale physical processes ignored at the resolution scale. They include small-scales eddies, topographic forcing or boundary layers turbulence for instance and are responsible both of an energy dissipation but also of local backscatters of energy. The introduction of random variables constitutes an appealing mechanism to model inverse energy cascade mechanism [23, 28, 35], in so far as they enable a phenomenological modeling of the uncertainties involved. Recently those models have regained a great interest for the modeling of geophysical flows [27, 36] in climate sciences (see also the thematic issue [32]). In fluid mechanics, Large eddies simulations (LES) and Reynolds average simulations (RANS) face also the very same question: how to model the action on the resolved component of the small scales of the flow. Numerous turbulence modeling used in the aforementioned methodologies rely on eddies viscosity concept to model the energy dissipation due to unresolved scales. Eddy viscosity concept dates back to the work of Boussinesq [3] and Prandl mixing length [33]. It relies on the hypothesis that the energy transfer from the resolved scales to the subgrid scales can be described in a similar way as the molecular viscosity mechanism. It is therefore not at all related to any uncertainty or error quantities. In models dealing explicitly

*Laboratoire Mathématiques, Image et Applications (MIA), Université de La Rochelle, Avenue Michel Crépeau 17042 La Rochelle, France (souleymane.kadri_harouna@univ-lr.fr).
†INRIA, Fluminance group, Campus universitaire de Beaulieu, 35042 Rennes, France (etienne.memin@inria.fr

with a probabilistic modeling of the small scales there is thus some incoherency in representing the dissipative mechanism attached to random component through an eddy viscosity assumption. In this work we will not make use on such hypothesis. Instead, we will rely on an expression of the subgrid stress tensor that explicitly depends on the uncertainty variance.

This subgrid model is properly derived from a general stochastic model of the fluid motion in which the fluid parcels displacement is decomposed in two components: a smooth differentiable function and an uncertainty function uncorrelated in time but correlated in space [30]. The whole displacement field is defined as an Eulerian description of the form:

$$\boldsymbol{U}(\boldsymbol{x},t) = \boldsymbol{w}(\boldsymbol{x},t)dt + \boldsymbol{\sigma}(\boldsymbol{x},t)d\tilde{\boldsymbol{B}}_t. \tag{1.1}$$

In this expression, $\boldsymbol{w} = (w_1, w_2, w_3)$, corresponds to the smooth resolved velocity component of the flow referred to as the *drift* or resolved component. It is assumed to be a deterministic differentiable function. The second component is a random component encoding the uncertainties we have on the flow. This uncertainty component, which is not differentiable in time, involves a diffusion tensor that has to be properly specified. Compared to the smooth drift, this component lives at a much smaller time scale. It is nevertheless defined at all the spatial scales. This approach is also close, in spirit, to the separation in term of a "coherent" component plus noise operated through adaptive wavelet basis [9, 10]. However, contrary to this approach relying on a Galerkin projection with an adaptive scale thresholding, our decomposition makes appear a diffusion tensor assembling the action of the unresolved uncertainty component on the resolved component.

The random field $\boldsymbol{U}(\boldsymbol{x},t)$, is assumed to follow a stochastic linear momentum conservation principle that is mainly derived from a stochastic version of the Reynolds transport theorem. This modified transport theorem is presented in the following section.

The paper is organized as follow. After a brief presentation of the stochastic Navier-Stokes system devised in [30], we describe a particular numerical scheme based on divergence free wavelets [15, 16].This particular type of wavelets together with the semi-implicit Euler scheme used to set up the discrete scheme are briefly presented in section 3. The stability of this numerical scheme is studied in section 4. The associated spatial discretization is detailed in section 5 and numerical results on the Green-Taylor vortex and on the reconnection of two vortex tubes are provided in section 6.

2. Navier-Stokes equation under uncertainty

As the system of Navier-Stokes equations we consider incorporates random uncertainties to describe unknown forcing or scale coarsening approximations, they constitute in essence a stochastic evolution system. Numerous methodological choices can be envisaged to constitute such a system. It is possible for instance to consider additional random forcing to a system of equations whose structure ensues from a deterministic formalization. This is the choice that has been the most often done since the work of Benssoussan [2]. Another choice, in the wake of Kraichnan's work [17], consists to close the large-scale representation in the Fourier space by relying on a Langevin stochastic representation [19, 21, 22]. Obviously the frontiers between these two methodologies are sometimes fuzzy, and numerous works rely on both of these strategies in order to setup the shape that should take the random variables evolution law [21, 35].

In this work, we shall rely on a different strategy that consists in directly defining the uncertainty as a location uncertainty on the resolution grid. A fluid particle location will be here defined only up to a Gaussian random field. The Navier-Stokes equations are then deduced from acceleration and second Newton's principle.

In a similar way as for the deterministic case, the main methodological tool used here is a stochastic version of the Reynolds transport theorem.

2.1. *Stochastic Reynolds transport theorem*

The Reynolds transport theorem provides the expression of the rate of change of a scalar function q within a material volume $\mathcal{V}(t)$ transported by the flow. Its extension to stochastic flows is given as [30]:

$$d\int_{\mathcal{V}(t)} q(\boldsymbol{x},t)d\boldsymbol{x} = \int_{\mathcal{V}(t)} \{dq_t + [\boldsymbol{\nabla}\cdot(q\boldsymbol{w}) + \frac{1}{2}\|\boldsymbol{\nabla}\cdot\boldsymbol{\sigma}\|^2 q - \sum_{i,j}\frac{1}{2}\frac{\partial^2}{\partial x_i \partial x_j}(a_{ij}q)_{|\boldsymbol{\nabla}\cdot\boldsymbol{\sigma}=0}]dt + \boldsymbol{\nabla}\cdot(q\boldsymbol{\sigma}d\tilde{\boldsymbol{B}}_t)\}d\boldsymbol{x}. \quad (2.1)$$

In this expression the first term is a time increment at fixed coordinates, $\boldsymbol{x}$, of the scalar quantity q. Let us note that this function is random and is not differentiable in time. The randomness of function q is an essential point in the derivation of this theorem as it requires to use a generalized form of Ito calculus – the Ito-Wentzell formula – adapted to the differentiation of the composition of two stochastic processes [20]. The last random term is built from a tempered representation of a Brownian map noted in a formal way through a convolution product $d\tilde{\boldsymbol{B}}_t = d\boldsymbol{B}_t \star \varphi_\nu$ and, $\boldsymbol{\sigma}_t$, a linear deterministic symmetric operator with null value outside the domain interior referred to as the diffusion tensor in the following. The random oscillating component is denoted:

$$\boldsymbol{\sigma}(\boldsymbol{x},t)d\tilde{\boldsymbol{B}}_t = \int \boldsymbol{\sigma}_t(\boldsymbol{x},\boldsymbol{y})d\tilde{\boldsymbol{B}}_t(\boldsymbol{y})d\boldsymbol{y}.$$

It is important to outline that an incompressibility condition on this component requires necessarily a divergence free diffusion tensor. The third term is related to the compression strength of the uncertainty field. The fourth term must be computed considering the diffusion tensor is divergence free. The tensor $\mathbf{a}(\boldsymbol{x})$ involved in this term is a matrix function associated to the diagonal elements of the covariance tensor. It corresponds hence to the uncertainty variance and is defined as:

$$a_{ij}(\boldsymbol{x},t) = \sum_k \sigma^\nu_{ik}(\boldsymbol{x},t)\sigma^\nu_{kj}(\boldsymbol{x},t), \quad (2.2)$$

where $\boldsymbol{\sigma}^\nu(\boldsymbol{x},\boldsymbol{y},t) = \boldsymbol{\sigma}(\boldsymbol{x},\bullet,t)\star\varphi_\nu(\boldsymbol{y})$ denotes a filtered version of the diffusion tensor along its second component. This rate of change formula is obtained from Ito-Wentzell differentiation of a function tending to the material volume characteristic function. The differentiation of the product of this characteristic function with the scalar function of interest, followed by a formal integration by part gives us the sought expression [30]. This relation allows us stating a mass conservation principle that accounts for the considered uncertainty on the fluid flow. Applying the previous transport theorem to the fluid density $\rho(\boldsymbol{x},t)$ and canceling this expression for arbitrary volumes, we get the following mass conservation constraint:

$$d\rho_t + \boldsymbol{\nabla}\cdot(\rho\boldsymbol{w})dt = \frac{1}{2}(\sum_{i,j}\frac{\partial^2}{\partial x_i\partial x_j}(a_{ij}\rho)_{|\boldsymbol{\nabla}\cdot\boldsymbol{\sigma}=0} - \frac{1}{2}\|\boldsymbol{\nabla}\cdot\boldsymbol{\sigma}\|^2\rho)dt - \boldsymbol{\nabla}\cdot(\rho\boldsymbol{\sigma}d\tilde{\boldsymbol{B}}_t). \quad (2.3)$$

For an incompressible fluid with constant density, canceling separately the slow deterministic terms and the rapid oscillating stochastic terms, and imposing to the whole deformation field (1.1) to be volume preserving, this system simplifies in a set of incompressibility relations:

$$\boldsymbol{\nabla}\cdot(\boldsymbol{\sigma}d\tilde{\boldsymbol{B}}_t) = 0, \quad \boldsymbol{\nabla}\cdot\boldsymbol{w} = 0, \quad \boldsymbol{\nabla}\cdot(\boldsymbol{\nabla}\cdot\mathbf{a}) = 0, \quad (2.4)$$

composed of two standard volume preserving constraints accompanied with a less intuitive additional volume preserving constraint on the divergence of the uncertainty variance tensor. For divergence free homogeneous isotropic random fields such as the Kraichnan random field [18] this last constraint is naturally satisfied as those fields are associated to a constant diagonal variance tensor. In this case the system reduces hence to the standard divergence free constraint.

For isochoric flow with varying density we get a mass conservation constraint of the form:

$$d\rho_t + \boldsymbol{\nabla}\rho\boldsymbol{w}dt - \frac{1}{2}\sum_{i,j}\frac{\partial^2}{\partial x_i x_j}(\rho a_{ij})dt = \boldsymbol{\nabla}\rho\sigma d\tilde{\boldsymbol{B}}_t. \tag{2.5}$$

In the case of the Kraichnan model the density variation involves a Laplacian diffusion and the density conditional expectation with respect to a given initial condition evolution comes to an intuitive advection diffusion equation. Let us note that the same kind of deterministic advection equation with an anisotropic diffusion is also obtained if the noise lies in the tangent plane of isodensity surfaces. This type of diffusion for the transport of a given scalar is often considered in geophysics to encode large scale mixing of stratified fluids. They are called isopycnal or isoneutral diffusion in this context [14].

2.2. *Linear momentum conservation*

The mass conservation constraint and the stochastic version of the Reynolds theorem allows us expressing the balance between the momentum and the forces:

$$d\int_{\mathcal{V}(t)}\rho(\boldsymbol{w}(\boldsymbol{x},t)dt + \boldsymbol{\sigma}(\boldsymbol{x},t)d\tilde{\boldsymbol{B}}_t)d\boldsymbol{x} = \int_{\mathcal{V}(t)}\boldsymbol{F}(\boldsymbol{x},t)d\boldsymbol{x}.$$

In this momentum equation, the differentiation in left hand term must be interpreted in a distribution sense (since the random term is non-differentiable). As for the forces in the right hand term, they are composed of standard deterministic forces such as the gravity force and forces acting on both the random and deterministic velocity components. For instance, the surface forces may be defined, as a direct extension of the deterministic, as:

$$\boldsymbol{\Sigma} = \int_{\mathcal{V}} -\boldsymbol{\nabla}(pdt + d\tilde{p}_t) + \mu(\Delta\boldsymbol{U} + \frac{1}{3}\boldsymbol{\nabla}(\boldsymbol{\nabla}\cdot\boldsymbol{U})).$$

In this expression μ is the dynamic viscosity, $p(\boldsymbol{x},t)$ denotes the deterministic contribution of the pressure and $d\tilde{p}_t$ is a zero mean stochastic pressure fluctuation attached to the random component of the velocity. The Navier-Stokes equations under uncertainty are obtained incorporating the mass preservation principle (2.3) and requiring that on both sides the same mathematical structures stand [30]. For a constant density and for a general divergence free (incompressible) uncertainty component, they read:

$$(\partial_t\boldsymbol{w} + \boldsymbol{w}\boldsymbol{\nabla}^T\boldsymbol{w} - \frac{1}{2}\sum_{i,j}\frac{\partial^2}{\partial x_i x_j}(a_{ij}\boldsymbol{w}))\rho = \rho\boldsymbol{g} - \boldsymbol{\nabla}p + \mu\Delta\boldsymbol{w}, \tag{2.6a}$$

$$\boldsymbol{\nabla}d\tilde{p}_t = -\boldsymbol{w}\boldsymbol{\nabla}^T\rho\boldsymbol{\sigma}d\tilde{\boldsymbol{B}}_t + \mu\Delta(\boldsymbol{\sigma}d\tilde{\boldsymbol{B}}_t), \tag{2.6b}$$

$$\boldsymbol{\nabla}\cdot(\boldsymbol{\sigma}d\tilde{\boldsymbol{B}}_t) = 0, \quad \boldsymbol{\nabla}\cdot\boldsymbol{w} = 0, \quad \boldsymbol{\nabla}\cdot(\boldsymbol{\nabla}\cdot\mathbf{a}) = 0. \tag{2.6c}$$

This system involves a first equation describing the evolution of the deterministic resolved component. It corresponds to the dynamics of the slow differentiable velocity component. Compared to the original Navier-Stokes formulation and similarly to the classical Reynolds decomposition, it includes an additional stress term that depends here on the resolved velocity component and on the uncertainty variance. The subsequent equations of this system denote a stochastic balance on the diffusion tensor and a mass conservation constraint respectively.

In the case of a divergence free isotropic model with constant density, we get a Navier-Stokes formulation with a constant eddy viscosity diffusivity coefficient :

$$(\frac{\partial \boldsymbol{w}}{\partial t}+\boldsymbol{w}\boldsymbol{\nabla}^T\boldsymbol{w}-\gamma\frac{1}{2}\Delta\boldsymbol{w})\rho=\rho\boldsymbol{g}-\boldsymbol{\nabla}p+\mu\Delta\boldsymbol{w},\ \boldsymbol{\nabla}\cdot\boldsymbol{w}=0, \tag{2.7}$$

where the diffusion is augmented by the noise variance. Note that in the previous non homogeneous model the diffusion term attached to the uncertainties cannot be directly related to the Boussinesq eddy viscosity formulation. However, it can be checked that for divergence free random field this term is globally dissipative as its energy is

$$\int_\Omega \boldsymbol{w}^T\sum_{i,j}\frac{\partial^2}{\partial x_i\partial x_j}(a_{ij}\boldsymbol{w})d\boldsymbol{x}=-\int_\Omega\|\nabla\boldsymbol{w}\|^2_{\mathbf{a}}d\boldsymbol{x}.$$

The subgrid stress tensor constitutes an anisotropic diffusion whose preferential directions of diffusion are given by the uncertainty variance. Setting the uncertainty diffusion tensor, $\boldsymbol{\sigma}$, or its variance tensor allows defining directly the subgrid diffusion term that has to be incorporated in the resolved drift component. For instance, considering uncertainties along iso-density surfaces provides immediately a clear justification of the isopycnal diffusion employed in oceanic circulation models [30]. The use also of constant eddy viscosity is also justified as the direct consequence of an isotropic homogeneous uncertainty component. Such an approach opens new perspectives for flow modeling that goes from *a priori* uncertainty specification to data based strategies. This framework, which does not rely neither on Reynolds averaging nor on spatial filtering concept, might be of great interest when uncertainties are prevalent as it is the case in geophysical flows or climate modeling. As another practical consequence, if one consider velocity fields supplied by particle image velocimetry methods, which are related to the true flow kinematics only up to a Gaussian uncertainty, then those measurements does not follow exactly the actual flow dynamics. Their physical interpretation should then be carried out with some care.

In the following we will experiment simple choices related in spirit to the scale similarity principles used to define subgrid stress tensor [1]. Before presenting the variance tensors we used, we present the numerical scheme we devised for the numerical simulation of the drift component.

3. A divergence-free wavelet numerical scheme for the drift component

The objective in this section is to provide a wavelet-based numerical discretization of the drift component equations of stochastic system (2.6). Precisely, we consider an incompressible homogeneous fluid satisfying:

$$\begin{cases}\frac{\partial \boldsymbol{w}}{\partial t}-\nu\Delta\boldsymbol{w}+\boldsymbol{w}\boldsymbol{\nabla}^T\boldsymbol{w}-\frac{1}{2}\sum_{i,j}\frac{\partial^2}{\partial x_ix_j}(a_{ij}\boldsymbol{w})+\boldsymbol{\nabla}p=\boldsymbol{f},\quad(\boldsymbol{x},t)\in\Omega\times]0,T[,\\ \boldsymbol{\nabla}\cdot\boldsymbol{w}=0,\quad\boldsymbol{x}\in\Omega,\\ \boldsymbol{w}(\boldsymbol{x},0)=\boldsymbol{w}_0,\quad\boldsymbol{x}\in\Omega,\end{cases} \tag{3.1}$$

where $\Omega \subset \mathbb{R}^d$ is a *regular* open bounded subset satisfying periodic boundary conditions and $\nu = \mu/\rho$ denotes the kinematic viscosity. Since the matrix $\boldsymbol{a}(\boldsymbol{x}, t)$ represents the covariance of the total flow, it is assumed to be set for all time with the following coercivity property:

$$\sum_{i,j} a_{ij}\xi_i\xi_j \geq \gamma|\xi|^2, \quad \forall\, \xi \in \mathbb{R}^d,$$

with $\gamma > 0$ a positive constant. In this case, for a *regular* solution $\boldsymbol{w}$, integration by part and Poincaré's inequality give:

$$\frac{1}{2}\frac{d}{dt}\int_\Omega |\boldsymbol{w}|^2 + \frac{\nu}{2}\int_\Omega |\boldsymbol{\nabla w}|^2 + \frac{1}{2}\int_\Omega \|\nabla \boldsymbol{w}\|^2_{\mathbf{a}} \leq C\|\boldsymbol{f}\|^2_{L^2(\Omega)^d}. \tag{3.2}$$

Again, using Poincaré and for $\alpha > 0$ we have:

$$\frac{d}{dt}\left(e^{\alpha t}\|\boldsymbol{w}\|^2_{L^2(\Omega)^d}\right) = e^{\alpha t}\left(\alpha\|\boldsymbol{w}\|^2_{L^2(\Omega)^d} + \frac{d}{dt}\|\boldsymbol{w}\|^2_{L^2(\Omega)^d}\right) \leq e^{\alpha t}\left(\frac{d}{dt}\|\boldsymbol{w}\|^2_{L^2(\Omega)^d} + \alpha C\int_\Omega |\boldsymbol{\nabla w}|^2\right). \tag{3.3}$$

Then, appropriately setting the value of α, we get the estimate:

$$\|\boldsymbol{w}\|^2_{L^2(\Omega)^d} \leq e^{-\alpha t}\|\boldsymbol{w}_0\|^2_{L^2(\Omega)^d} + \int_0^t e^{(s-\alpha t)}\|\boldsymbol{f}\|_{H^{-1}(\Omega)^d} ds. \tag{3.4}$$

Without forcing term ($\boldsymbol{f} = 0$), from (3.2) and (3.4), we deduce that the *regular* solution $\boldsymbol{w}$ is uniformly bounded and its energy decays exponentially in time:

$$\|\boldsymbol{w}\|^2_{L^2(\Omega)^d} \leq C(\boldsymbol{w}_0) \quad \text{and} \quad \|\boldsymbol{w}\|^2_{L^2(\Omega)^d} \leq e^{-\alpha t}C(\boldsymbol{w}_0). \tag{3.5}$$

For numerical stability constraints, it is important for any numerical discretization associated to (3.1) to satisfy condition similar to (3.4) or (3.5). The objective of the forthcoming sections is to provide a wavelet-based numerical scheme of this type for the spatial discretization. The temporal discretization will rely on a finite difference method. Moreover, we will show that a semi-implicit Euler scheme with explicit treatment of the non linear term $\boldsymbol{w}\boldsymbol{\nabla}^T\boldsymbol{w}$ and the diffusion term $\frac{1}{2}\sum_{i,j}\frac{\partial^2}{\partial x_i x_j}(a_{ij}\boldsymbol{w})$ is stable under a particular CFL type condition. In the following we start first describing the spatial discretization and then we present the temporal evolution scheme.

3.1. *Spatial discretization*

For the spatial discretization of (3.1), a Galerkin method is used. Since the resolved velocity $\boldsymbol{w}$ is incompressible, to incorporate this constraint directly, a divergence-free wavelet basis is considered [8, 15]. Then, at a fixed spatial resolution $j > 0$, the approximate solution $\boldsymbol{w}_j$ is defined by:

$$\boldsymbol{w}_j(\boldsymbol{x}, t) = \sum_{|\boldsymbol{j}|\leq j, \boldsymbol{k}} \boldsymbol{d}_{\boldsymbol{j},\boldsymbol{k}}(t)\Psi^{\mathrm{div}}_{\boldsymbol{j},\boldsymbol{k}}(\boldsymbol{x}), \quad \boldsymbol{\nabla}\cdot\Psi^{\mathrm{div}}_{\boldsymbol{j},\boldsymbol{k}} = 0, \quad j \in \mathbb{N}, \tag{3.6}$$

where $\{\Psi^{\mathrm{div}}_{\boldsymbol{j},\boldsymbol{k}}\}_{\boldsymbol{j},\boldsymbol{k}\in\mathbb{Z}^d}$ is the divergence-free wavelet basis associated to the velocity functional space. For details on the construction of a such wavelet basis, we refer the reader to [8, 15] and references therein.

Let $\mathbf{V}_j$ be the multiresolution analysis spaces associated to the divergence-free wavelets basis $\{\Psi^{\text{div}}_{\boldsymbol{j},\boldsymbol{k}}\}_{\boldsymbol{j},\boldsymbol{k}\in\mathbb{Z}^d}$. For any j, the space $\mathbf{V}_j$ is a finite dimensional space, thus all the norm on $\mathbf{V}_j$ are equivalent. In particular, we have:

$$\lim_{j\to+\infty} \|\boldsymbol{w}-\boldsymbol{w}_j\|_{L^2(\Omega)^d} = 0, \quad \|\boldsymbol{w}_j\|_{L^2(\Omega)^d} \lesssim \|\boldsymbol{w}\|_{L^2(\Omega)^d},$$

together with the Bernstein and Jackson inequalities:

$$\|\boldsymbol{w}_j\|_{H^s(\Omega)^d} \lesssim 2^{js}\|\boldsymbol{w}_j\|_{L^2(\Omega)^d} \qquad \text{and} \qquad \inf_{\boldsymbol{w}_j\in\mathbf{V}_j} \|\boldsymbol{w}-\boldsymbol{w}_j\|_{L^2(\Omega)^d} \lesssim 2^{-js}\|\boldsymbol{w}\|_{H^s(\Omega)^d}. \tag{3.7}$$

In this context, the mesh size is given as $\delta x = 2^{-j}$, where $j > 0$ denotes the spatial resolution. We note that (3.6) provides a time and space scale separation and since the wavelet basis $\{\Psi^{\text{div}}_{\boldsymbol{j},\boldsymbol{k}}\}_{\boldsymbol{j},\boldsymbol{k}\in\mathbb{Z}^d}$ is explicitly defined, the unknown consists of the set of coefficients $\boldsymbol{d}_{\boldsymbol{j},\boldsymbol{k}}(t)$. To compute the coefficients $\boldsymbol{d}_{\boldsymbol{j},\boldsymbol{k}}(t)$ we must invert the mass and stiffness matrices of the wavelet basis $\{\Psi^{\text{div}}_{\boldsymbol{j},\boldsymbol{k}}\}_{\boldsymbol{j},\boldsymbol{k}\in\mathbb{Z}^d}$. For the 2D case, details on this step are provided in Section 3.4, the generalization to higher dimension is analogous.

3.2. *Temporal discretization*

For the time discretization of (3.1), we employ a similar methods as the one proposed in [8]. Without loss of generality, we will assume in the following that there is no external forcing: $\boldsymbol{f} = 0$. The projection of (2.6a) onto the divergence-free function space leads to:

$$\frac{\partial \boldsymbol{w}}{\partial t} - \nu\Delta\boldsymbol{w} = \mathbb{P}[-\boldsymbol{w}\boldsymbol{\nabla}^T\boldsymbol{w} + \frac{1}{2}\sum_{i,j}\frac{\partial^2}{\partial x_i x_j}(a_{ij}\boldsymbol{w})], \tag{3.8}$$

where $\mathbb{P}$ denotes the Leray projector: the orthogonal projector from $L^2(\Omega)^d$ onto the divergence-free function space $\mathcal{H}_{div}(\Omega) = \{\boldsymbol{u}\in L^2(\Omega)^d \ : \ \boldsymbol{\nabla}\cdot\boldsymbol{u} = 0\}$. The projector $\mathbb{P}$ is in general explicitly defined in Fourier domain. In the present work, the computation of this projector is done though the projection onto the divergence-free wavelet basis $\{\Psi^{\text{div}}_{\boldsymbol{j},\boldsymbol{k}}\}$, see [8, 15].

It can be observed that equation (3.8) corresponds to a heat equation with a source term given by $\mathbb{P}[-\boldsymbol{w}\boldsymbol{\nabla}^T\boldsymbol{w} + \frac{1}{2}\sum_{i,j}\frac{\partial^2}{\partial x_i x_j}(a_{ij}\boldsymbol{w})]$. Classical numerical schemes used for the heat kernel discretization can hence be borrowed. Sticking to an implicit Euler scheme with a fixed time step δt and setting $\boldsymbol{w}^n(\boldsymbol{x}) \simeq \boldsymbol{w}_j(n\delta t, \boldsymbol{x})$ with $n\in\mathbb{N}$, leads to:

$$(I - \nu\delta t\Delta)\boldsymbol{w}^{n+1} = \boldsymbol{w}^n - \delta t\mathbb{P}[\boldsymbol{w}^n\boldsymbol{\nabla}^T\boldsymbol{w}^n - \frac{1}{2}\sum_{i,j}\frac{\partial^2}{\partial x_i x_j}(a^n_{ij}\boldsymbol{w}^n)]. \tag{3.9}$$

The pressure p can be classically recovered through the Helmholtz-Hodge decomposition of the nonlinear and the anisotropic diffusion terms:

$$\boldsymbol{w}\boldsymbol{\nabla}^T\boldsymbol{w} - \frac{1}{2}\sum_{i,j}\frac{\partial^2}{\partial x_i x_j}(a_{ij}\boldsymbol{w}) = \mathbb{P}[\boldsymbol{w}\boldsymbol{\nabla}^T\boldsymbol{w} - \frac{1}{2}\sum_{i,j}\frac{\partial^2}{\partial x_i x_j}(a_{ij}\boldsymbol{w})] - \nabla p.$$

The convergence and the computational efficiency of the discrete scheme (3.9) highly depends on the time step value. In the following section we establish a necessary stability condition for the method convergence. This condition will allow us to fix a maximal value for the time step in practice.

3.3. *Stability of the semi-implicit Euler scheme*

In this section, we show that the semi-implicit Euler scheme (3.9) is stable in a sense that will be specified. Assuming the matrix $\boldsymbol{a}(\boldsymbol{x},t)$ is given and bounded on $\Omega\times[0,T]$:

$$\|a_{ij}\|_{L^\infty(\Omega\times[0,T])}\leq C,$$

we prove the following proposition:

Proposition 3.1.
Whenever the kinematic viscosity ν, the anisotropic diffusion coefficients a_{ij}, the time step δt and the mesh size $\delta x=2^{-j}$ satisfy:

$$\nu\geq\frac{1}{2}\|a_{ij}\|_{L^\infty(\Omega\times[0,T])}\qquad\text{and}\qquad\frac{\delta t}{\delta x^d}\leq C,\tag{3.10}$$

then there exists $\lambda(\nu,\Omega)>0$, positive constant independent of δt and δx, such that the solution $\boldsymbol{w}^n$ given by (3.9) *is stable in the following sense:*

$$\|\boldsymbol{w}^{n+1}\|^2_{L^2(\Omega)^d}\leq(1+\delta t\lambda(\nu,\Omega))^{-n}\|\boldsymbol{w}^0\|^2_{L^2(\Omega)^d}+C_0\sum_{k=0}^{n-1}(1+\delta t\lambda(\nu,\Omega))^{k-n},\tag{3.11}$$

where C_0 is a constant depending on ν, $\boldsymbol{w}^0$ and a_{ij}.

The relation defined by (3.11) is the discrete analogous of (3.4) and uniform bound for $\|\boldsymbol{w}^n\|^2_{L^2(\Omega)^d}$ similar to (3.5) can be deduced. To prove this stability property of the iterates we need the following intermediate lemma.

Lemma 3.1.
If the parameters ν, a_{ij}, δt and $\delta x=2^{-j}$ satisfy the condition of (3.10)*, the solution $\boldsymbol{w}^n$ given by* (3.9) *remains bounded in the following sense:*

$$\|\boldsymbol{w}^n\|^2_{L^2(\Omega)^d}\leq C(\boldsymbol{w}^0,a_{ij}),\ n=0,\cdots,N\tag{3.12}$$

$$\sum_{k=1}^{N}\|\boldsymbol{w}^k-\boldsymbol{w}^{k-1}\|^2_{L^2(\Omega)^d}\leq C(\boldsymbol{w}^0,a_{ij}),\tag{3.13}$$

$$\delta t\sum_{k=1}^{N}\|\nabla\boldsymbol{w}^k\|^2_{L^2(\Omega)^{d\times d}}\leq C(\boldsymbol{w}^0,a_{ij}).\tag{3.14}$$

where $C(\boldsymbol{w}^0,a_{ij})>0$ is a constant depending on the initial data.

Lemma 3.1 is analogous to lemma 5.3 of [38]. Very similar arguments can be used for its proof, this proof is provided in Appendix A. Let us now prove Proposition 3.1.

Proof.
Taking $2\boldsymbol{w}^{n+1}$ as a test function in (3.9), for each term we obtain:

$$\begin{aligned}&2\int_\Omega(1-\nu\delta t\Delta)\boldsymbol{w}^{n+1}\cdot\boldsymbol{w}^{n+1}-2\int_\Omega\boldsymbol{w}^n\cdot\boldsymbol{w}^{n+1}=\\&\|\boldsymbol{w}^{n+1}\|^2_{L^2(\Omega)^d}-\|\boldsymbol{w}^n\|^2_{L^2(\Omega)^d}+2\delta t\nu\|\nabla\boldsymbol{w}^{n+1}\|^2_{L^2(\Omega)^{d\times d}}+\|\boldsymbol{w}^{n+1}-\boldsymbol{w}^n\|^2_{L^2(\Omega)^d},\end{aligned}$$

and

$$\int_\Omega \mathbb{P}[\frac{\partial^2}{\partial x_i \partial x_j}(a_{ij}\boldsymbol{w}^n)] \cdot \boldsymbol{w}^{n+1} \leq \|a_{ij}\|_{L^\infty(\Omega\times[0,T])}\|\nabla \boldsymbol{w}^{n+1}\|_{L^2(\Omega)^{d\times d}}\|\nabla \boldsymbol{w}^n\|_{L^2(\Omega)^{d\times d}}.$$

due to the incompressibility constraint:

$$\boldsymbol{\nabla}\cdot(\boldsymbol{\nabla}\cdot\boldsymbol{a}) = 0.$$

For the non linear term, since

$$\int_\Omega (\boldsymbol{w}^n\cdot\nabla)\boldsymbol{w}^n\cdot\boldsymbol{w}^n = -\frac{1}{2}\int_\Omega(\nabla\cdot\boldsymbol{w}^n)|\boldsymbol{w}^n|^2 = 0,$$

one obtains:

$$2\int_\Omega (\boldsymbol{w}^n\cdot\nabla)\boldsymbol{w}^n\cdot(\boldsymbol{w}^{n+1}-\boldsymbol{w}^n) \leq 2\|\boldsymbol{w}^n\|_{L^\infty(\Omega)^d}\|\nabla\boldsymbol{w}^n\|_{L^2(\Omega)^d}\|\boldsymbol{w}^{n+1}-\boldsymbol{w}^n\|_{L^2(\Omega)^d}.$$

As we are in a finite dimensional space, in addition to (3.7), we have:

$$\|\boldsymbol{w}^n\|_{L^\infty(\Omega)^d} \leq 2^{jd/2}\|\boldsymbol{w}^n\|_{L^2(\Omega)^d}, \tag{3.15}$$

then, we get:

$$2\|\boldsymbol{w}^n\|_{L^\infty}\|\nabla\boldsymbol{w}^n\|_{L^2(\Omega)^d}\|\boldsymbol{w}^{n+1}-\boldsymbol{w}^n\|_{L^2(\Omega)^d} \leq 2.2^{jd/2}\|\boldsymbol{w}^n\|_{L^2(\Omega)^d}\|\nabla\boldsymbol{w}^n\|_{L^2(\Omega)^{d\times d}}\|\boldsymbol{w}^{n+1}-\boldsymbol{w}^n\|_{L^2(\Omega)^d}.$$

Thus

$$\begin{aligned}&\|\boldsymbol{w}^{n+1}\|^2_{L^2(\Omega)^d} - \|\boldsymbol{w}^n\|^2_{L^2(\Omega)^d} + 2\delta t\nu\|\nabla\boldsymbol{w}^{n+1}\|^2_{L^2(\Omega)^{d\times d}} + \|\boldsymbol{w}^{n+1}-\boldsymbol{w}^n\|^2_{L^2(\Omega)^d}\\ &\leq 2\delta t 2^{\frac{jd}{2}}\|\boldsymbol{w}^n\|_{L^2(\Omega)^d}\|\nabla\boldsymbol{w}^n\|_{L^2(\Omega)^{d\times d}}\|\boldsymbol{w}^{n+1}-\boldsymbol{w}^n\|_{L^2(\Omega)^d} + \delta t\|a_{ij}\|_{L^\infty(\Omega\times[0,T])}\|\nabla\boldsymbol{w}^{n+1}\|_{L^2(\Omega)^{d\times d}}\|\nabla\boldsymbol{w}^n\|_{L^2(\Omega)^{d\times d}},\end{aligned}$$

and Young's inequality leads to:

$$\begin{aligned}&\|\boldsymbol{w}^{n+1}\|^2_{L^2(\Omega)^d} - \|\boldsymbol{w}^n\|^2_{L^2(\Omega)^d} + \delta t\nu\|\nabla\boldsymbol{w}^{n+1}\|^2_{L^2(\Omega)^{d\times d}} + \frac{1}{2}\|\boldsymbol{w}^{n+1}-\boldsymbol{w}^n\|^2_{L^2(\Omega)^d}\\ &\leq 2\delta t^2 2^{jd}\|\boldsymbol{w}^n\|^2_{L^2(\Omega)^d}\|\nabla\boldsymbol{w}^n\|^2_{L^2(\Omega)^{d\times d}} + \frac{\delta t\|a_{ij}\|^2_{L^\infty(\Omega\times[0,T])}}{4\nu}\|\nabla\boldsymbol{w}^n\|^2_{L^2(\Omega)^{d\times d}}.\end{aligned} \tag{3.16}$$

Now we fixed δt small enough such that:

$$2\delta t 2^{jd}C(\boldsymbol{w}^0, a_{ij}) \leq \frac{1}{2}(\nu - \frac{\|a_{ij}\|^2_{L^\infty(\Omega\times[0,T])}}{4\nu}). \tag{3.17}$$

Since $\|\boldsymbol{w}^n\|^2_{L^2(\Omega)^d} \leq C(\boldsymbol{w}^0, a_{ij})$, by Lemma 3.1 and from (3.16) we deduce that:

$$\|\boldsymbol{w}^{n+1}\|^2_{L^2(\Omega)^d} - \|\boldsymbol{w}^n\|^2_{L^2(\Omega)^d} + \delta t\nu\|\nabla\boldsymbol{w}^{n+1}\|^2_{L^2(\Omega)^{d\times d}} \leq \frac{\delta t}{2}(\nu + \frac{\|a_{ij}\|^2_{L^\infty(\Omega\times[0,T])}}{4\nu})\|\nabla\boldsymbol{w}^n\|^2_{L^2(\Omega)^{d\times d}}. \tag{3.18}$$

Using Poincaré's inequality, we get:

$$\|\boldsymbol{w}^{n+1}\|^2_{L^2(\Omega)^d} - \|\boldsymbol{w}^n\|^2_{L^2(\Omega)^d} + \frac{\delta t\nu}{C(\Omega)^2}\|\boldsymbol{w}^{n+1}\|^2_{L^2(\Omega)^d} \leq \frac{\delta t}{2}(\nu + \frac{\|a_{ij}\|^2_{L^\infty(\Omega\times[0,T])}}{4\nu})\|\nabla\boldsymbol{w}^n\|^2_{L^2(\Omega)^{d\times d}}. \tag{3.19}$$

We set $\lambda(\nu,\Omega) = \frac{\nu}{C(\Omega)^2}$. Then, the sequence A_n defined by:

$$A_n = (1+\delta t\lambda(\nu,\Omega))^n\|\boldsymbol{w}^n\|^2_{L^2(\Omega)^{d\times d}}, \tag{3.20}$$

satisfies:

$$A_{n+1} - A_n = (1+\delta t\lambda(\nu,\Omega))^n \left(\|\boldsymbol{w}^{n+1}\|^2_{L^2(\Omega)^d} - \|\boldsymbol{w}^{n}\|^2_{L^2(\Omega)^d} + \delta t\lambda(\nu,\Omega)\|\boldsymbol{w}^{n+1}\|^2_{L^2(\Omega)^d} \right)$$
$$\leq (1+\delta t\lambda(\nu,\Omega))^n \frac{\delta t}{2}(\nu + \frac{\|a_{ij}\|^2_{L^\infty(\Omega\times[0,T])}}{4\nu})\|\nabla \boldsymbol{w}^n\|^2_{L^2(\Omega)^{d\times d}}.$$

Summation over n leads to:

$$A_n - A_0 \leq \sum_{k=0}^{n-1}(1+\delta t\lambda(\nu,\Omega))^k \frac{\delta t}{2}(\nu + \frac{\|a_{ij}\|^2_{L^\infty(\Omega\times[0,T])}}{4\nu})\|\nabla \boldsymbol{w}^k\|^2_{L^2(\Omega)^{d\times d}}.$$

Again, from Lemma 3.1 we have:

$$\delta t\|\nabla \boldsymbol{w}^n\|^2_{L^2(\Omega)^{d\times d}} \leq C(\boldsymbol{w}^0, a_{ij}), \quad \forall\ n = 0, 1, \cdots,$$

thus:

$$A_n - A_0 \leq C_0 \sum_{k=0}^{n-1}(1+\delta t\lambda(\nu,\Omega))^k, \tag{3.21}$$

with $C_0 = \frac{1}{2}(\nu + \frac{\|a_{ij}\|^2_{L^\infty(\Omega\times[0,T])}}{4\nu})C(\boldsymbol{w}^0, a_{ij})$. Replacing A_n by its expression (3.20) ends the proof. □

To complete this section, we analyze now the behavior of the discretization error as δt goes to zero and $j > 0$ goes to infinity:

$$\boldsymbol{e}^n = \boldsymbol{w}(\boldsymbol{x}, t_n) - \boldsymbol{w}^n,$$

where $t_n = n\delta t$ denotes the corresponding discrete time and $\boldsymbol{w}(t,x)$ is an exact smooth solution of (2.6a). Replacing $\boldsymbol{w}^n$ by its expression $\boldsymbol{w}^n = \boldsymbol{w}(\boldsymbol{x}, t_n) - \boldsymbol{e}^n$ in (3.9) reads:

$$\frac{\boldsymbol{e}^{n+1} - \boldsymbol{e}^n}{\delta t} - \nu\Delta \boldsymbol{e}^{n+1} + \mathbb{P}[-(\boldsymbol{e}^n\cdot\nabla)\boldsymbol{e}^n - \frac{1}{2}\sum_{ij}\frac{\partial^2}{\partial x_i \partial x_j}(a_{ij}\boldsymbol{e}^n)] = \boldsymbol{\epsilon}^{n+1} - \mathbb{P}[(\boldsymbol{w}(\boldsymbol{x},t_n)\cdot\nabla)\boldsymbol{e}^n + (\boldsymbol{e}^n\cdot\nabla)\boldsymbol{w}(\boldsymbol{x},t_n)], \tag{3.22}$$

where $\boldsymbol{\epsilon}^n$ denotes the consistency error related to the injection of the exact solution into the numerical scheme (3.9):

$$\frac{\boldsymbol{w}(\boldsymbol{x},t_{n+1}) - \boldsymbol{w}(\boldsymbol{x},t_n)}{\delta t} - \nu\Delta \boldsymbol{w}(\boldsymbol{x},t_{n+1}) + \mathbb{P}[(\boldsymbol{w}(\boldsymbol{x},t_n)\cdot\nabla)\boldsymbol{w}(\boldsymbol{x},t_n) - \frac{1}{2}\sum_{ij}\frac{\partial^2}{\partial x_i\partial x_j}(a_{ij}\boldsymbol{w}(\boldsymbol{x},t_n))] = \boldsymbol{\epsilon}^{n+1}. \tag{3.23}$$

From (3.23), we infer that: $\boldsymbol{\epsilon}^n \in H^{-1}(\Omega)$ and it is divergence free: $\boldsymbol{\nabla}\cdot\boldsymbol{\epsilon}^n = 0$. Then, with similar arguments to those used for the proof of Proposition 3.1, one can show that:

$$\|\boldsymbol{e}^{n+1}\|^2_{L^2(\Omega)^d} - \|\boldsymbol{e}^n\|^2_{L^2(\Omega)^d} + \delta t\nu\|\nabla\boldsymbol{e}^{n+1}\|^2_{L^2(\Omega)^{d\times d}} \leq 2\delta t^2 2^{jd}\left(\|\boldsymbol{e}^n\|^2_{L^2(\Omega)^d} + \|\boldsymbol{w}(t_n)\|^2_{L^2(\Omega)^d}\right)\|\nabla\boldsymbol{e}^n\|^2_{L^2(\Omega)^{d\times d}}$$
$$+ \frac{\delta t\|a_{ij}\|^2_{L^\infty(\Omega\times[0,T])}}{4\nu}\|\nabla\boldsymbol{e}^n\|^2_{L^2(\Omega)^{d\times d}} + 2\delta t 2^{jd/2}\|\boldsymbol{e}^n\|_{L^2(\Omega)^d}\|\boldsymbol{w}(t_n)\|_{L^2(\Omega)^d}\|\nabla\boldsymbol{e}^{n+1}\|_{L^2(\Omega)^{d\times d}}$$
$$+ 2\delta t\|\boldsymbol{\epsilon}^{n+1}\|_{H^{-1}(\Omega)}\|\boldsymbol{e}^{n+1}\|_{L^2(\Omega)^d}. \tag{3.24}$$

Otherwise, using (3.9), we get:

$$-\nu\Delta\boldsymbol{w}(\boldsymbol{x},t_{n+1}) = -\partial_t\boldsymbol{w}(t_{\boldsymbol{x},n+1}) - \mathbb{P}[(\boldsymbol{w}(\boldsymbol{x},t_{n+1})\cdot\nabla)\boldsymbol{w}(\boldsymbol{x},t_{n+1}) - \frac{1}{2}\sum_{ij}\frac{\partial^2}{\partial x_i\partial x_j}(a_{ij}\boldsymbol{w}(\boldsymbol{x},t_{n+1}))], \tag{3.25}$$

thus,

$$\begin{aligned}\boldsymbol{\epsilon}^{n+1} = -\partial_t\boldsymbol{w}(\boldsymbol{x},t_{n+1}) + \frac{\boldsymbol{w}(\boldsymbol{x},t_{,n+1}) - \boldsymbol{w}(\boldsymbol{x},t_n)}{\delta t} + \mathbb{P}[(\boldsymbol{w}(\boldsymbol{x},t_n)\cdot\nabla)\boldsymbol{w}(\boldsymbol{x},t_n) - (\boldsymbol{w}(\boldsymbol{x},t_{n+1})\cdot\nabla)\boldsymbol{w}(\boldsymbol{x},t_{n+1})] \\ - \frac{1}{2}\mathbb{P}[\sum_{ij}\frac{\partial^2}{\partial x_i\partial x_j}(a_{ij}(\boldsymbol{x},t_n)\boldsymbol{w}(\boldsymbol{x},t_n) - a_{ij}(\boldsymbol{x},t_{n+1})\boldsymbol{w}(\boldsymbol{x},t_{n+1}))].\end{aligned}$$

Since we assume that $\boldsymbol{w}$ is regular enough, we have:

$$\begin{aligned}\boldsymbol{\epsilon}^{n+1} = \frac{1}{\delta t}\int_{t_n}^{t_{n+1}}(t-t_n)\partial_{tt}\boldsymbol{w}(\boldsymbol{x},t)dt - \mathbb{P}\left[\int_{t_n}^{t_{n+1}}\partial_t[(\boldsymbol{w}(\boldsymbol{x},t)\cdot\nabla)\boldsymbol{w}(t)]dt\right] \\ + \frac{1}{2}\sum_{ij}\mathbb{P}\left[\int_{t_n}^{t_{n+1}}\frac{\partial^2}{\partial x_i\partial x_j}(\partial_t[a_{ij}\boldsymbol{w}(\boldsymbol{x},t)])dt\right],\end{aligned} \tag{3.26}$$

and this gives:

$$\begin{aligned}\delta t\sum_n\|\boldsymbol{\epsilon}^{n+1}\|^2_{H^{-1}(\Omega)} \leq \delta t^2\|\partial_{tt}\boldsymbol{w}(t)\|^2_{L^2(0,T;H^{-1}(\Omega))} + 3\delta t\|\partial_t[(\boldsymbol{w}(t)\cdot\nabla)\boldsymbol{w}(t)]\|^2_{L^2(0,T;H^{-1}(\Omega))} \\ + \frac{3\delta t}{2}\|\frac{\partial^2}{\partial x_i\partial x_j}(\partial_t[a_{ij}\boldsymbol{w}(t)])\|^2_{L^2(0,T;H^{-1}(\Omega))},\end{aligned}$$

and by definition we have:

$$\|\boldsymbol{e}^n\|^2_{L^2(\Omega)^d} \leq 2\left(\|\boldsymbol{w}^n\|^2_{L^2(\Omega)^d} + \|\boldsymbol{w}(t_n)\|^2_{L^2(\Omega)^d}\right), \quad \|\nabla\boldsymbol{e}^n\|^2_{L^2(\Omega)^2} \leq 2\left(\|\nabla\boldsymbol{w}^n\|^2_{L^2(\Omega)^{d\times d}} + \|\nabla\boldsymbol{w}(t_n)\|^2_{L^2(\Omega)^{d\times d}}\right). \tag{3.27}$$

From (3.24) and recalling that the right-hand terms of inequalities (3.27) are bounded by constants depending only on the initial data, there exists hence a suitable constant depending only on the initial data such that:

$$\|\boldsymbol{e}^{n+1}\|^2_{L^2} - \|\boldsymbol{e}^n\|^2_{L^2} + \frac{\delta t\nu}{4}\|\nabla\boldsymbol{e}^{n+1}\|^2_{L^2} \leq (\delta t + \delta x^{d/2})C(\boldsymbol{w}^0, a_{ij}, \Omega). \tag{3.28}$$

Summation of (3.28) over n shows that:

$$\max_n\|\boldsymbol{e}^n\|^2_{L^2(\Omega)^d} \xrightarrow[\delta t\to 0,\delta x\to 0]{} 0. \tag{3.29}$$

and hence the semi-implicit temporal numerical scheme (3.9) converges.

3.4. *Practical computational details of the divergence free numerical scheme*

For sake of simplicity, we present in this section practical details on the implementation of our divergence-free wavelet numerical scheme in the particular case of two dimensional space: $\Omega = [0,1]^2$. The extension to the 3D space is direct and poses no difficulty [8]. We start by the construction of divergence-free wavelet basis. To

construct divergence-free wavelet in $(L^2(\Omega))^2$, one needs first to set up two multi-resolution analyses of $L^2(0,1)$ generated by the spaces V_j^1 and V_j^0 linked by differentiation:

$$\frac{d}{dx}V_j^1 = V_j^0.$$

In this case, it can be shown [24] that the associated wavelet generators ψ^1 and ψ^0 satisfy: $(\psi^1)' = 4\psi^0$. Then, the divergence-free wavelet generator is constructed as:

$$\Psi^{div} = \mathbf{curl}[\psi^1 \otimes \psi^1] = 4 \begin{pmatrix} \psi^1 \otimes \psi^0 \\ -\psi^0 \otimes \psi^1 \end{pmatrix}. \tag{3.30}$$

This divergence-free wavelet is contained in the standard multi-resolution analysis of $(L^2(\Omega))^2$ provided by spaces $\mathbf{V}_j = (V_j^1 \otimes V_j^0) \times (V_j^0 \otimes V_j^1)$, it provides hence fast divergence-free wavelet transform, see [8, 16] for details. This fast transform allows us to compute the divergence-free wavelet coefficients of $\boldsymbol{w}^n = (w_1^n, w_2^n)$ from those of its decomposition on the wavelet basis associated to $\mathbf{V}_j$ and conversely:

$$w_1^n = \sum_{|\boldsymbol{j}|\leq j,\boldsymbol{k}} d_{\boldsymbol{j},\boldsymbol{k}}^{1,n} \psi_{j_1,k_1}^1 \otimes \psi_{j_2,k_2}^0 \quad \text{and} \quad w_2^n = \sum_{|\boldsymbol{j}|\leq j,\boldsymbol{k}} d_{\boldsymbol{j},\boldsymbol{k}}^{2,n} \psi_{j_1,k_1}^0 \otimes \psi_{j_2,k_2}^1. \tag{3.31}$$

Moreover, in (3.9) to compute the coefficients of $\boldsymbol{w}^{n+1}$ from those of $\boldsymbol{w}^n$, one needs to invert the matrix corresponding to operator $(1 - \delta t\nu\Delta)$. To avoid computing this inverse at each time step, we use the method described in [5], which relies on the heat kernel operator factorization. This method pertains to the framework of alternated direction implicit methods. More precisely, for a given $\alpha \in \mathbb{R}$, in two dimension we have:

$$(1 - \alpha\Delta) \approx (1 - \alpha\frac{\partial^2}{\partial x^2})(1 - \alpha\frac{\partial^2}{\partial y^2}) + O(\alpha^2). \tag{3.32}$$

Using this technique in (3.9), we have only to invert the matrix of a one dimensional operator $(1 - \delta t\nu\frac{\partial^2}{\partial x^2})$, and this is done only once before starting the time integration.

Then, taking the wavelets $\psi_{j_1,k_1}^1 \otimes \psi_{j_2,k_2}^0$ and $\psi_{j_1,k_1}^0 \otimes \psi_{j_2,k_2}^1$ as test functions in (3.9), we get the following linear systems of wavelet matrices of coefficients:

$$\mathcal{A}_{\delta t}^1[d_{\boldsymbol{j},\boldsymbol{k}}^{1,n+1}]\mathcal{A}_{\delta t}^0 = \mathcal{M}^1[d_{\boldsymbol{j},\boldsymbol{k}}^{1,n}]\mathcal{M}^0 + \delta t\mathcal{M}^1[f_{\boldsymbol{j},\boldsymbol{k}}^{1,n}]\mathcal{M}^0 \tag{3.33}$$

and

$$\mathcal{A}_{\delta t}^0[d_{\boldsymbol{j},\boldsymbol{k}}^{2,n+1}]\mathcal{A}_{\delta t}^1 = \mathcal{M}^0[d_{\boldsymbol{j},\boldsymbol{k}}^{2,n}]\mathcal{M}^1 + \delta t\mathcal{M}^0[f_{\boldsymbol{j},\boldsymbol{k}}^{2,n}]\mathcal{M}^1, \tag{3.34}$$

where $\mathcal{A}_{\delta t}^i$ and $\mathcal{M}^i$ respectively correspond to stiffness matrix of operator $(1 - \delta t\nu\frac{\partial^2}{\partial x^2})$ and mass matrix on the one-dimensional wavelet bases of $\{V_j^i\}_{i=0,1}$. The elements of these matrices are computed analytically by solving en eigenvalue problem [16]. The source term $[f_{\boldsymbol{j},\boldsymbol{k}}^{1,n}]$ and $[f_{\boldsymbol{j},\boldsymbol{k}}^{2,n}]$ correspond to the wavelet coefficients of the orthogonal projection onto the divergence-free function space of the non linear term and the anisotropic diffusion term:

$$\boldsymbol{f}^n = -\mathbb{P}[(\boldsymbol{w}^n \cdot \nabla)\boldsymbol{w}^n - \frac{1}{2}\sum_{ij}\frac{\partial^2}{\partial x_i \partial x_j}(a_{ij}\boldsymbol{w}^n)], \tag{3.35}$$

where the spatial derivatives are computed using finite difference method at the grid points.

The whole resolution method can be summarized as follows. Starting from $\boldsymbol{w}^0(x) = \boldsymbol{w}(\boldsymbol{x}, 0)$, compute its wavelet coefficients $[d^{1,0}_{\boldsymbol{j},\boldsymbol{k}}]$ and $[d^{2,0}_{\boldsymbol{j},\boldsymbol{k}}]$ on $\mathbf{V}_j = (V^1_j \otimes V^0_j) \times (V^0_j \otimes V^1_j)$ and for $0 \leq n \leq N$, repeat

Step 1: Using finite difference method, compute the term

$$\tilde{\boldsymbol{f}}^n = -(\boldsymbol{w}^n \cdot \nabla)\boldsymbol{w}^n - \frac{1}{2}\sum_{ij} \frac{\partial^2}{\partial x_i \partial x_j}(a_{ij}\boldsymbol{w}^n)$$

Step 2: Compute the divergence-free wavelet coefficients $[d^{div,n}_{\boldsymbol{j},\boldsymbol{k}}] = \mathbb{P}(\tilde{\boldsymbol{f}}^n)$ by:

$$\mathcal{M}^1[\tilde{f}^{1,n}_{\boldsymbol{j},\boldsymbol{k}}]\tilde{\mathcal{A}}^0 - (\tilde{\mathcal{A}}^0)^T[\tilde{f}^{2,n}_{\boldsymbol{j},\boldsymbol{k}}]\mathcal{M}^1 = \mathcal{M}^1[d^{div,n}_{\boldsymbol{j},\boldsymbol{k}}]\mathcal{R}^1 + \mathcal{R}^1[d^{div,n}_{\boldsymbol{j},\boldsymbol{k}}]\mathcal{M}^1$$

where $\mathcal{R}^1$ is the stiffness matrix of wavelet basis $\{\psi^1_{j,k}\}$, its terms correspond to $\langle(\psi^d_{j,k})', (\psi^1_{j',k'})'\rangle$ and the terms of $\tilde{\mathcal{A}}^0$ correspond to $\langle\psi^0_{j,k}, (\psi^d_{j',k'})'\rangle$.

Step 3: Compute $[f^{1,n}_{\boldsymbol{j},\boldsymbol{k}}]$ and $[f^{2,n}_{\boldsymbol{j},\boldsymbol{k}}]$ from $[d^{div,n}_{\boldsymbol{j},\boldsymbol{k}}]$ using the change of basis between $\{(\psi^1_{\boldsymbol{j},\boldsymbol{k}})'\}$ and $\{\psi^0_{\boldsymbol{j},\boldsymbol{k}}\}$.

Step 4: Find $[d^{1,n+1}_{\boldsymbol{j},\boldsymbol{k}}]$ and $[d^{2,n+1}_{\boldsymbol{j},\boldsymbol{k}}]$ solution of

$$\mathcal{A}^1_{\delta t}[d^{1,n+1}_{\boldsymbol{j},\boldsymbol{k}}]\mathcal{A}^0_{\delta t} = \mathcal{M}^1[d^{1,n}_{\boldsymbol{j},\boldsymbol{k}}]\mathcal{M}^0 + \delta t\mathcal{M}^1\boldsymbol{f}^n_1\mathcal{M}^0$$

$$\mathcal{A}^0_{\delta t}[d^{2,n+1}_{\boldsymbol{j},\boldsymbol{k}}]\mathcal{A}^1_{\delta t} = \mathcal{M}^0[d^{2,n}_{\boldsymbol{j},\boldsymbol{k}}]\mathcal{M}^1 + \delta t\mathcal{M}^0\boldsymbol{f}^n_2\mathcal{M}^1$$

As the matrices $\mathcal{A}^1_{\delta t}$ and $\mathcal{A}^0_{\delta t}$ are inverted once for all before starting the algorithm, step 4 corresponds thus only to a matrix multiplication. Let J be the maximal space resolution considered, then the theoretical complexity of Step 4 is $O(2^{3J})$. Step 2 is solved with a preconditioned conjugate gradient method, then its theoretical complexity is $O(2^{3J})$ and step 3 is a change of basis, whose complexity is linear. We deduce that the theoretical complexity of the method is about $O(2^{3J})$. In practice, this theoretical complexity can be improved using adaptive methods and coherent structure extraction methods, see [6, 9, 10, 39].

4. Numerical results

This section presents the results of several numerical simulations that have been carried out to validate the model. One of the main advantages of the uncertainty formalism we propose lies in the great flexibility of the anisotropic diffusion coefficients specification. The variance uncertainty tensor, $\boldsymbol{a}$, can be fixed from *a priori* knowledge either on the uncertainty's variance or on the uncertainty diffusion tensor. These knowledge may be directly inferred from the approximations considered to constitute the model. Aspect ratio simplifications and/or not perfectly known boundary conditions could probably be used to introduce preferred direction of the variance uncertainty tensor. The uncertainty variance could as well be learned from small-scale measurements or specified from empirical local statistics of the resolved component. Let us point out nevertheless, that whatever the choice carried out, the explicit discretization of anisotropic diffusion term in the temporal discrete scheme (3.9) induces a viscosity dependent CFL type condition that must be carefully taken into account. In

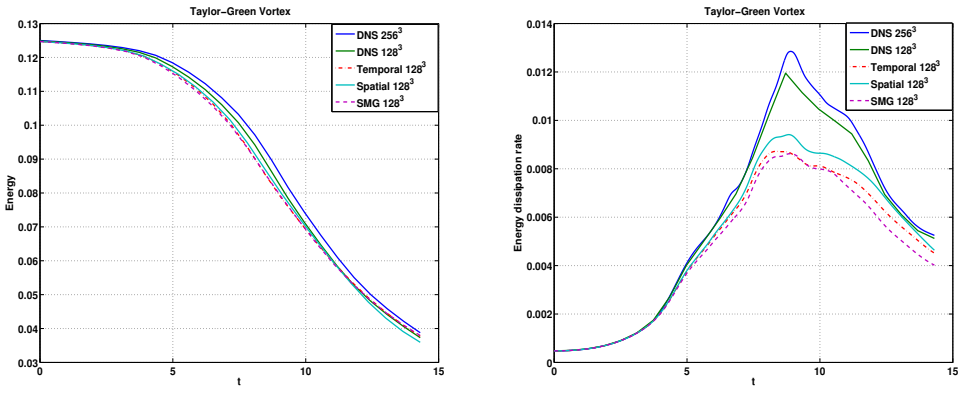

Figure 1. Evolution of the dimensionless energy $\mathcal{E}(t)$ (left) and its dissipation rate $\epsilon(t) = -\frac{d\mathcal{E}}{dt}$ (right) as a function of the dimensionless time.

this study we implement a very simple strategy that consists in defining $\boldsymbol{a}(n\delta t, \boldsymbol{x})$ as local empirical covariances of the resolved velocity fields $\boldsymbol{w}(\boldsymbol{x})^n$:

$$a_{ij}(\boldsymbol{x}, t) = C\delta t < (w_i(\boldsymbol{y}) - \mu_i(\boldsymbol{x}, t))(w_j(\boldsymbol{y}) - \mu_j(\boldsymbol{x}, t)) >_{\boldsymbol{y}\in\mathcal{W}(\boldsymbol{x},t)},$$

where $\mu_i(\boldsymbol{x}, t)$ is the empirical mean on a spatial or temporal window $\mathcal{W}(\boldsymbol{x}, t)$ and $C > 0$, fixed as $C = \frac{1}{|\mathcal{W}(\boldsymbol{x},t)|}$ to normalize the window's volume. The empirical averaging is computed either spatially over a small $(3\times3\times3)$ window centered around point $(\boldsymbol{x}, t)$ or temporally at point $\boldsymbol{x}$, over the time interval $[(n-2)\delta t, n\delta t]$. In the following, they are referred to as the spatial and temporal uncertainty covariances respectively.

To evaluate the numerical accuracy and effectiveness of these models, two numerical benchmark simulations have been conducted. The first one concerns the Taylor-Green vortex [4] simulation at moderated Reynolds number $Re = 1600$. This flow becomes rapidly turbulent with creation of small-scale structures, followed by a decay phase similar to a decaying homogeneous turbulence. It is probably one of the simplest flow to study the production of small-scale eddies due to vorticity increase and vortex stretching mechanism. Due to non-linear interaction, this flow freely develops an homogeneous turbulence from an initial analytical solution of conter-rotating vortices at a single length scale and regularly disposed on the 3D grid. For this flow, we compared the two uncertainty covariance models to a Smagorinsky-Lilly model with constant value $C_s = (0.1 - 0.2)$ referred to as SMG solution. Figure 1 shows time evolution of both total kinetic energy and the energy dissipation-rate associated to the different solutions. These curves can be compared to a reference solution computed through a direct numerical simulation (DNS) of the incompressible Navier-Stokes equations on a 256^3 grid points. This corresponds to $j = 8$ wavelet space resolution in our simulation setup. The reference DNS solution on 128^3 grid corresponds to wavelet multiresolution projection onto those grids of the reference solution. They are hence computed from a spatial cut-off. As can be noted on Figure 2, it does not correspond to a spectral filtering, the energy of this projection intrinsically depends on the wavelet generator. Wavelets offer from that point of view an optimal choice with respect to a scale space energy representation due to their fine space-frequency localization property. However, they provide at lower resolution grid a spectrum which departs significantly, at medium scales, from the reference spectrum. This departure shows clearly the inhability of a direct projection

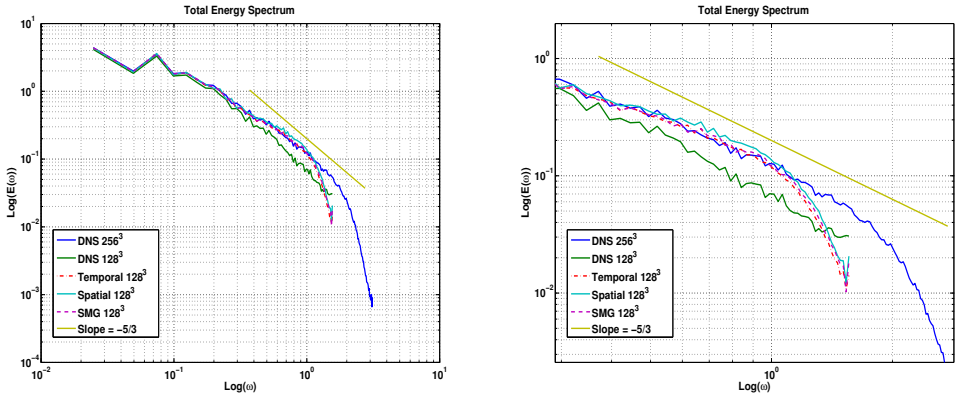

Figure 2. Different solutions total energy spectrums (left) and zoom in at the tail (right), for the dimensionless time $t \approx 9$.

on the low-resolution subspace spanned by the divergence-free wavelet basis we used to represent large eddies representations. At the opposite, a low resolution divergence-free wavelet basis implementation accompanied by the proposed uncertainty diffusion tensor enables to get a much more satisfying solution. Regarding their energy spectra both correlation forms provides close results. Compared to the results obtained with the Smagorinsky-Lilly eddy viscosity subgrid tensor, we observe on figure 1 that the solution provided both by the temporal and spatial correlation tensor have both higher kinetic energy except at the end of the turbulence decay where the Smagorinsky-Lily model performs better and reach the energy level provided by the corresponding wavelets truncation. The evolution of the dissipation rate along time shows a better behavior of the spatial correlation subgrid model. It provides much better results than the Smagorinsky subgrid tensor. The temporal correlation performs only slightly better than the Smagorinsky model. Note that the dissipation peak is slightly anticipated in time for the temporal correlation, whereas for the spatial correlation and the Smagorinsky model it is well aligned with the DNS results. On the same curve, it can be observed that the Smagorinsky model and the temporal correlation show a greater difficulty to produce small-scale velocity gradients. The spatial correlation appears thus to be a better subgrid model for this flow.

On Figure 3, we show the plot of Q iso-surfaces, colored by the gradient magnitude, for the dimensionless time $t \approx 9$ (that corresponds almost to the time at which the dissipation peak occurs), where:

$$Q = -\frac{1}{2} \sum_{i,j} \frac{\partial w_i}{\partial x_j} \frac{\partial w_j}{\partial x_i}.$$

The sub spatial domain of Figure 3 corresponds to $(0, \pi)^3$. It can be readily observed that the solution computed using the spatial covariance exhibits smaller vortex structures in comparison both to the temporal covariance uncertainty model and the Smagorinsky model. Let us note that for both models the solutions resemble very much to the corresponding projected DNS. Compared to results of the literature [4, 11], these first results are very encouraging.

The second experience concerns vortex tubes collision simulation. The initial condition is a sinusoidal perturbation of two counter-rotating vortex tubes of circular section, parallel and located by either sides of

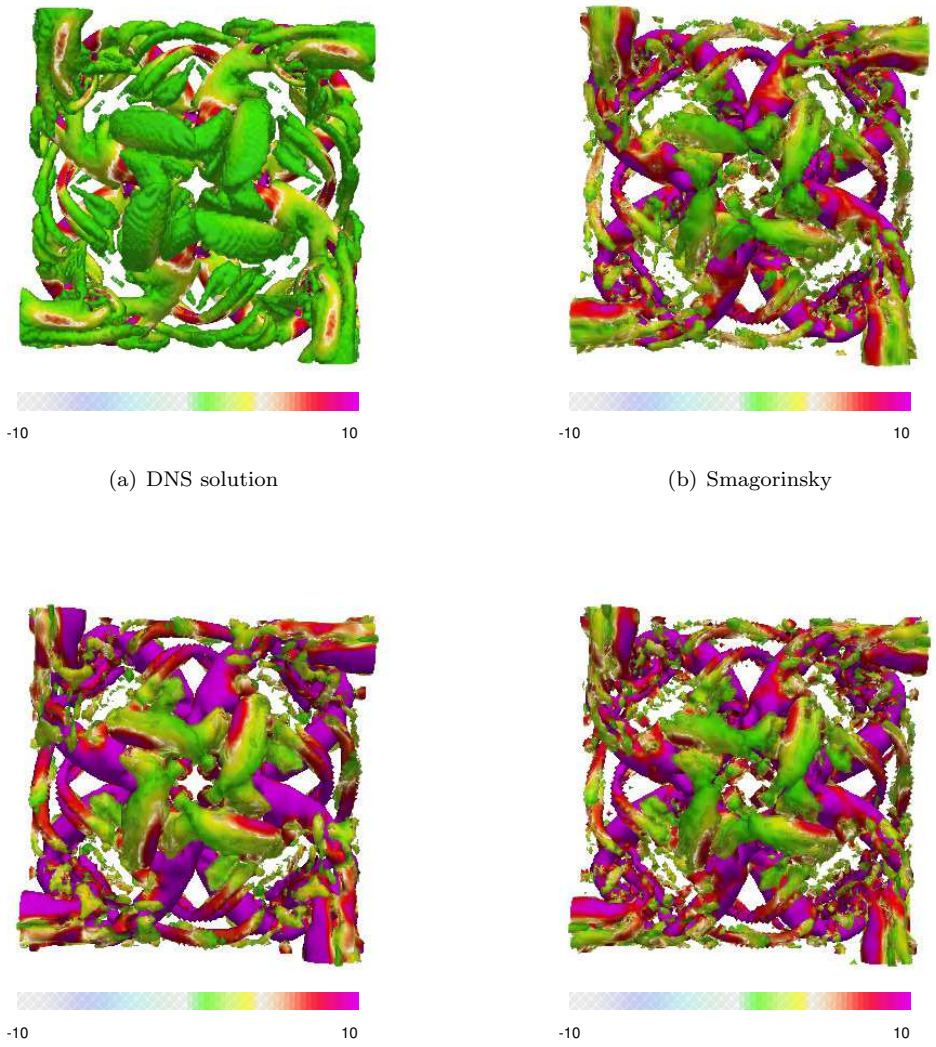

(a) DNS solution (b) Smagorinsky

(c) Temporal correlation (d) Spatial correlation

Figure 3. Iso-surfaces $Q = 1$ for the dimensionless time $t \approx 9$: (a) 256^3 grid points DNS solution, (b) Smagorinsky solution onto 128^3 grid points, (c) solution computed with temporal covariance on 128^3 grid points and (d) solution computed with spatial covariance on 128^3 grid points.

the plane $y = \pi$. The Reynolds number has been set to $Re = 3500$. Unlike to the Green-Taylor vortex, this flow is non-isotropic and it represents a classical situation where vorticity blow-up is suspected [29]. It is also known that the Smagorinsky subgrid model does not work well on this flow because of its strong diffusion

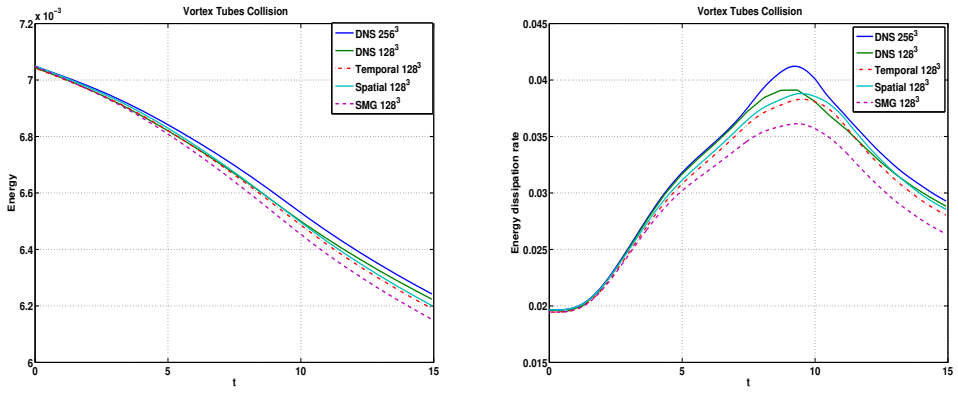

Figure 4. Evolution of the dimensionless energy $\mathcal{E}(t)$ (left) and its dissipation rate $\epsilon(t) = -\frac{d\mathcal{E}}{dt}$ (right) as a function of the dimensionless time.

in the reconnection region [7]. This phenomenon is confirmed by Figure 4 where the different solutions total energy and energy dissipation rate time evolution are plotted. The time evolution of the kinetical energy shows that the Smagorinsky is associated to solutions of significantly lower energy. Until the dissipation peak the kinetic energy of both the spatial and temporal correlations are closed to the optimal truncated wavelets low-resolution representation. After the dissipation peak the produced solution are lower to the low-resolution wavelets projection. For the three subgrid models (i.e Smagorinsky, spatial and temporal correlation models) the time at which the dissipation occurs is slightly delayed.

Figure 5 and Figure 6 show plots of iso-surfaces of Q magnitude for the dimensionless time $t = 10$ and $t = 15$ respectively. As can be seen from these figures, the solutions computed using both uncertainty models have more energy and present smaller structures compared to those computed with Smagorinsky subgrid model.

5. Conclusion

In this paper we have described a decomposition of the Navier-Stokes equation in terms of a resolved deterministic component and a random uncertainty component figuring the unresolved flow component. This decomposition leads to a new large scale representation paradigm. For its numerical simulation, we proposed an efficient numerical discrete scheme that relies on divergence-free wavelet. Efficient wavelets transforms allowed us to implement efficiently this scheme with Matlab on conventional computers. In addition, we presented some results on the consistency and the stability of this wavelet numerical schemes.

Such large-scale representation has been assessed for a Taylor-Green vortex flow and a flow generated by a vortex pair instability. The results obtained for a local empirical uncertainty model computed on a local spatial window of the resolved component leads to very encouraging results when compared to state-of-the-art large-scale simulations of these flows. Within the continuation of this study, we will investigate the derivation of similar model for geophysical flow equations and its use in the case of physical boundary conditions. This situation is more realist and it is known that many sub-grid models do not perform well in the presence of a wall. We wish also to investigate the use of variational data assimilation technique to determine the uncertainty

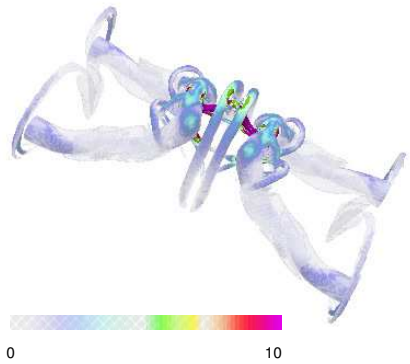

(a) DNS solution

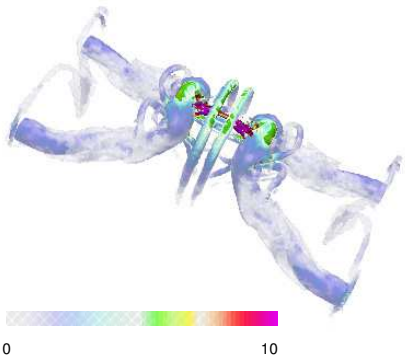

(b) Smagorinsky

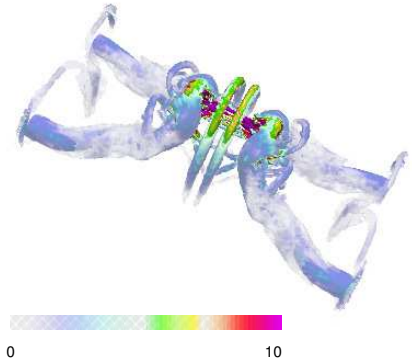

(c) Temporal correlation

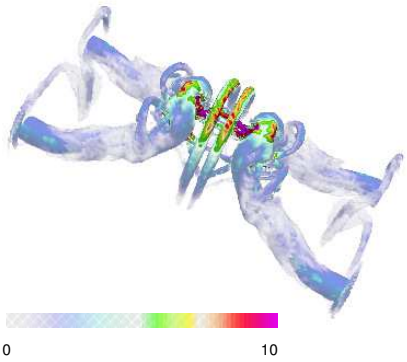

(d) Spatial correlation

Figure 5. Iso-surfaces of Q magnitude for the dimensionless time $t \approx 10$: (a) 256^3 grid points DNS solution, (b) Smagorinsky solution onto 128^3 grid points, (c) solution computed with temporal covariance on 128^3 grid points and (d) solution computed with spatial covariance on 128^3 grid points.

sub-grid tensor from image data observation operator. This study will be the subject of a new forthcoming paper.

Appendix A. Proof of Lemma 1

To prove Lemma 3.1 it is sufficient to verify that if (3.17) holds, then by induction we must have:

$$\|\boldsymbol{w}^n\|_{L^2}^2 + \frac{1}{2}\sum_{k=1}^{n}\|\boldsymbol{w}^k - \boldsymbol{w}^{k-1}\|_{L^2}^2 + \frac{\delta t}{2}(\nu - \frac{\|a_{ij}\|_{L^\infty}^2}{4\nu})\sum_{k=1}^{n}\|\nabla \boldsymbol{w}^k\|_{L^2}^2 \leq C(\boldsymbol{w}^0, a_{ij}), \tag{A.1}$$

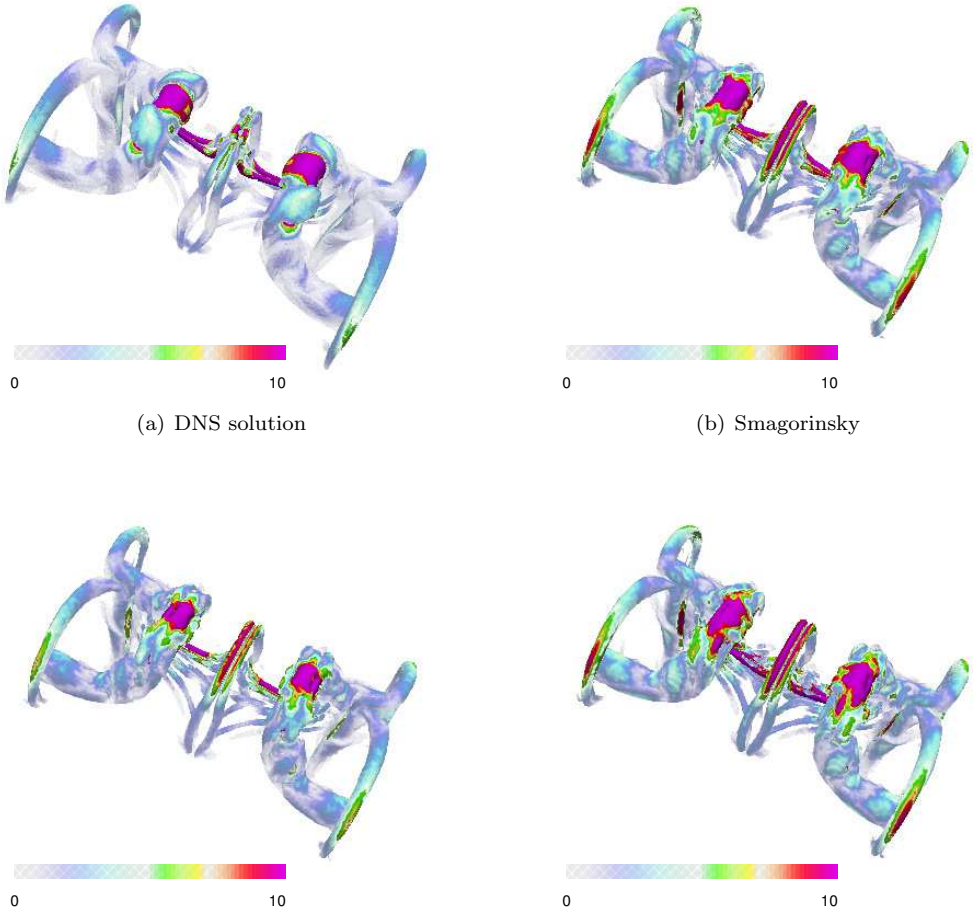

(a) DNS solution (b) Smagorinsky

(c) Temporal correlation (d) Spatial correlation

Figure 6. Iso-surfaces of Q magnitude for the dimensionless time $t = 15$: (a) 256^3 grid points DNS solution, (b) Smagorinsky solution onto 128^3 grid points, (c) solution computed with temporal covariance on 128^3 grid points and (d) solution computed with spatial covariance on 128^3 grid points.

where

$$C(\boldsymbol{w}^0, a_{ij}) = \|\boldsymbol{w}^0\|_{L^2}^2 + 2\delta t^2 2^{jd} \|\boldsymbol{w}^0\|_{L^2}^2 \|\nabla \boldsymbol{w}^0\|_{L^2}^2 + \frac{\|a_{ij}\|_{L^\infty}^2}{4\nu} \|\nabla \boldsymbol{w}^0\|_{L^2}^2. \tag{A.2}$$

Indeed, (3.16) gives this relation for $n = 1$. Suppose (A.1) true for order $n-1$, then we have:

$$2\delta t^2 2^{jd} \sum_{k=1}^{n-1} \|\boldsymbol{w}^k\|_{L^2}^2 \|\nabla \boldsymbol{w}^k\|_{L^2}^2 \leq 2\delta t^2 2^{jd} C(\boldsymbol{w}^0, a_{ij}) \sum_{k=1}^{n-1} \|\nabla \boldsymbol{w}^k\|_{L^2}^2, \tag{A.3}$$

and from (3.17) we get:

$$2\delta t^2 2^{jd} \sum_{k=1}^{n-1} \|\boldsymbol{w}^k\|_{L^2}^2 \|\nabla \boldsymbol{w}^k\|_{L^2}^2 \leq \frac{\delta t}{2}(\nu - \frac{\|a_{ij}\|_{L^\infty}^2}{4\nu}) \sum_{k=1}^{n} \|\nabla \boldsymbol{w}^k\|_{L^2}^2. \tag{A.4}$$

Otherwise, adding inequalities (3.16) for $k = 1, \cdots, n$; reads:

$$\begin{aligned} &\|\boldsymbol{w}^n\|_{L^2}^2 + \frac{1}{2}\sum_{k=1}^{n} \|\boldsymbol{w}^k - \boldsymbol{w}^{k-1}\|_{L^2}^2 + \delta t(\nu - \frac{\|a_{ij}\|_{L^\infty}^2}{4\nu}) \sum_{k=1}^{n} \|\nabla \boldsymbol{w}^k\|_{L^2}^2 \\ &\leq C(\boldsymbol{w}^0, a_{ij}) + 2\delta t^2 2^{jd} \sum_{k=1}^{n-1} \|\boldsymbol{w}^k\|_{L^2}^2 \|\nabla \boldsymbol{w}^k\|_{L^2}^2. \end{aligned} \tag{A.5}$$

Putting (A.4) in (A.5), we get the statements of (A.1) at order n and this proves Lemma 3.1.

References

1. Bardina, J., Ferziger, J.H. & Reynolds W.C., Improved subgrid scale models for large eddy simulation, *AIAA*, **80**, 1357.
2. Bensoussan, A. & Temam, R., 1973, Equations stochastique du type Navier-Stokes. *J. Funct. Anal.* **13**.
3. Boussinesq, J., 1877, Essai sur la théorie des eaux courantes. Mémoires présentés par divers savants à l'Académie des Sciences, 23 (1): 1–680.
4. Brachet, M., Meiron, D., Orszag, S., Nickel, B., Morf, R. & Frisch, U., 1983, Small-scale structure of the taylor-green vortex *J. Fluid. Mech.* **130(6)**, 411–452.
5. Charton, P.& Perrier, V., 1996, A Pseudo-Wavelet Scheme for the Two-Dimensional Navier-Stokes Equations *Comp. Appl. Math.* **15**,137–157.
6. Cohen, A. 2003 *Numerical Analysis of Wavelet Methods*, Elsevier.
7. Cottet, G.-H., Jiroveanu, D. & Michaux, B., 2003 ,Vorticity dynamics and turbulence models for large-eddy simulations *M2AN* **37**, 187–207.
8. Deriaz, E. & Perrier, V., 2006, Divergence-free and curl-free wavelets in 2D and 3D, application to turbulent flows *J. of Turbulence* **7(3)**, 1–37.
9. Farge, M., Pellegrino, G. & Schneider, K., 2001, Coherent vortex extraction in 3D turbulent flows using orthogonal wavelets *Phys. Rev. Lett.* **87**, 054501.
10. Farge, M., Schneider, K. & Kevlahan, N., 1999, Non-Gaussianity and coherent vortex simulation for two-dimensional turbulence using an adaptative orthogonal wavelet basis*Phys. Fluids* **11**, 2187–2201.
11. Fauconnier, D., De Langhe, C. & Dick, E., 2009, A family of dynamic finite difference schemes for large-eddy simulation *J. of Comp. Physics* **228**, 1853–1884.
12. Flandoli, F., 2008, *SPDE in hydrodynamics*, *Lecture Notes in Math*, vol. 1942, chap. An intoduction to 3D stochastic Navier Stokes, 51–150. Berlin: Springer Verlag.
13. Gawedzky, K. & Kupiainen, A., 1995, Anomalous scaling of the passive scalar. *Physical review letters* **75**, 3834–3837.
14. Gent, P. & McWilliams, J., 1990, Isopycnal mixing in ocean circulation models. *J. Phys. Oceanogr.* **20**, 150–155.
15. Kadri-Harouna, S. & Perrier, V., 2011, Helmholtz-Hodge Decomposition on $[0,1]^d$ by Divergence-free and Curl-free Wavelets, *J.-D Boissonat et (Eds), Curves and Surfaces, 2011, LNCS 6920, Springer Verlag Berlin Heidelberg*, 311–329.

16. Kadri-Harouna, S. & Perrier, V., 2013, Effective construction of divergence-free wavelets on the square *J. of Computational and Applied Math.* **240** 74–86.
17. Kraichnan, R., 1959, The structure of isotropic turbulence at very high Reynolds numbers. *J. Fluid Mech.*, **5**, 477–543.
18. Kraichnan, R.,1968, Small-scale structure of a randomly advected passive scalar. *Phys. Rev. Lett.* **11**, 945–963.
19. Kraichnan, R., 1970, Small-scale structure of a randomly advected passive scalar. *Phys. Rev. Lett.* **11**, 945–963.
20. Kunita, H., *Stochastic flows and stochastic differential equations*, , 1990, (Cambridge University Press), Cambridge, UK.
21. Laval J.-P , Dubrulle B. and McWilliams J.C., 2006, Langevin models of turbulence: Renormalization group, distant interaction algorithms or rapid distortion theory? *Phys. of Fluids*, **15(5)**, 1327-1339.
22. Leith, C., 1971, Atmospheric predictability and two-dimensional turbulence. *J. Atmos. Sci.* 1971, **28**, 145–161.
23. Leith, C., 1990, Stochastic backscatter in a subgrid-scale model: plane shear mixing layer. *Phys. of Fluids*, **2(3)**, 1521–1530.
24. Lemarié-Rieusset, P. G., 1992, Analyses multi-résolutions non orthogonales, commutation entre projecteurs et dérivation et ondelettes vecteurs à divergence nulle. *Revista Matemática Iberoamericana* **8**, 221–236.
25. Lilly, D., 1966, On the application of the eddy viscosity concept in the inertial subrange of turbulence. *Tech. Rep.* 123. NCAR.
26. Majda, A. & Kramer, P., 1999, Simplified models for turbulent diffusion:theory, numerical modelling, and physical phenomena. *Physics report* **314**, 237–574.
27. Majda, A., Timofeyev, I. and Vanden Eijnden, E., 1999, Models for stochastic climate prediction. *PNAS*, **96(26)**, 14687–14691.
28. Mason, P.J. and Thomson, D.J., 1989, Stochastic backscatter in large-eddy simulations of boundary layers, *J. of Fluid Mech.,* **242**, 51–78.
29. Melander, M., V. & Zabusky, N., 1989, Three Dimensional Vortex Tube Reconnection. Morphology for Orthogonal Offset Tubes. *Physica D,* 37.
30. Mémin, E., 2014, Fluid flow dynamics under location uncertainty. *Geophysical & Astrophysical Fluid Dynamics* , http://hal.inria.fr/hal-00852874, in press.
31. Mikulevicius, R. & Rozovskii, B.L., 2004, Stochastic Navier-Stokes equations for turbulent flows. *SIAM J. Math. Anal.* **35** (4), 1250–1310.
32. Palmer, T. & Williams, P., 2008, Theme Issue 'Stochastic physics and climate modelling' *Phil. Trans. R. Soc.,* **366(1875)**.
33. Prandtl, L., 1925, Bericht Ãijber Untersuchungen zur ausgebildeten Turbulenz *Z. Angew. Math, Meth.***5**, 136-139..
34. Sagaut, P., 2005, *Large-eddy simulation for incompressible flow - An introduction, third edition*. Springer-Verlag, Scientic Computation series.
35. Schumann, U., 1995, Stochastic backscatter of turbulence energy and scalar variance by random subgrid-scale fluxes. *Proc. R. Soc. Lond. A* **451**, 293–318 .
36. Slingo, J. and Palmer, T., 2011, Uncertainty in weather and climate prediction. *Phil. Trans. R. Soc.* A , **369**, 4751–4767.
37. Smagorinsky, J., 1963, General circulation experiments with the primitive equation: I. the basic experiment.

Monthly Weather Review **91**, 99–165.
38. Temam, R., 1977, *Navier Stokes Equations*, North Holland, New York.
39. Vasilyev, O.V., de Stefano, G., Goldstein, D. & Kevlahan, N. K.-R., 2008, Lagrangian dynamic SGS model for Stochastic Coherent Adaptive Large Eddy Simulation *J. Turbulence* **11**, 1-14.